JASS Journal of Astronomy and Space Sciences

A Substorm Injection Event and the Radiation Belt Structure Observed by Space Radiation Detectors onboard Next Generation Small Satellite-1 (NEXTSat-1)

Ji-Hyeon Yoo[1], Dae-Young Lee[1†], Eojin Kim[2], Hoonkyu Seo[2], Kwangsun Ryu[2], Kyung-Chan Kim[1], Kyoungwook Min[3], Jongdae Sohn[4], Junchan Lee[2], Jongho Seon[5], Kyung-In Kang[2], Seunguk Lee[1], Jaeheung Park[4], Goo-Hwan Shin[2], SungOg Park[2]

[1]Department of Astronomy and Space Science, Chungbuk National University, Cheongju 28644, Korea
[2]Satellite Technology Research Center, Korea Advanced Institute of Science and Technology, Daejeon 34141, Korea
[3]Department of Physics, Korea Advanced Institute of Science and Technology, Daejeon 34141, Korea
[4]Korea Astronomy and Space Science Institute, Daejeon 34055, Korea
[5]School of Space Research, Kyung Hee University, Yongin 17104, Korea

In this paper, we present observations of the Space Radiation Detectors (SRDs) onboard the Next Generation Small Satellite-1 (NEXTSat-1) satellite. The SRDs, which are a part of the Instruments for the study of Stable/Storm-time Space (ISSS), consist of the Medium-Energy Particle Detector (MEPD) and the High-Energy Particle Detector (HEPD). The MEPD can detect electrons, ions, and neutrals with energies ranging from 20 to 400 keV, and the HEPD can detect electrons over an energy range from 0.35 to 2 MeV. In this paper, we report an event where particle flux enhancements due to substorm injections are clearly identified in the MEPD A observations at energies of tens of keV. Additionally, we report a specific example observation of the electron distributions over a wide energy range in which we identify electron spatial distributions with energies of tens to hundreds of keV from the MEPD and with energy ranging up to a few MeV from the HEPD in the slot region and outer radiation belts. In addition, for an ~1.5-year period, we confirm that the HEPD successfully observed the well-known outer radiation belt electron flux distributions and their variations in time and L shell in a way consistent with the geomagnetic disturbance levels. Last, we find that the inner edge of the outer radiation belt is mostly coincident with the plasmapause locations in L, somewhat more consistent at subrelativistic energies than at relativistic energies. Based on these example events, we conclude that the SRD observations are of reliable quality, so they are useful for understanding the dynamics of the inner magnetosphere, including substorms and radiation belt variations.

Keywords: energetic particles, substorm injection, radiation belt, low-earth orbit observations

1. INTRODUCTION

The Next Generation Small Satellite-1 (NEXTSat-1) launched in December 2018 is a sun-synchronous polar-orbiting satellite with an altitude of 575 km and an orbital inclination of 97°. Having a mass of approximately 100 kg and dimensions of 600 × 600 × 800 mm, the spacecraft has an orbital speed of approximately 7.6 km/s and an orbital period of approximately 96 minutes (Shin et al. 2014). NEXTSat-1 consists of two scientific payloads: Instruments for the study of Stable/Storm-time Space (ISSS) for space science and the Near-Infrared Imaging Spectrometer for Star formation history (NISS) for astronomy. The ISSS instrument is composed of Space Radiation Detectors (SRDs) and Space Plasma Detectors (SPDs). The SRDs comprise the Medium-Energy Particle Detector (MEPD) and High-Energy Particle

Detector (HEPD), and the SPDs comprise the Langmuir Probe (LP), Retarding Potential Analyzer (RPA), and Ion Drift Meter (IDM) (See Sohn et al. (2018) and Kim et al. (2020) for details of the ISSS instruments). We do not deal with the data from SPDs here, the details of which are described in Choi et al. (2014) and Lee et al. (2018).

The SRDs used in this paper mainly operate in the subauroral and auroral regions during nighttime. They are designed to understand source and loss mechanisms in the radiation belts and the ring current region by observing particles trapped in the geomagnetic field or precipitating into the Earth's atmosphere (Kim et al. 2020). The MEPD can detect electrons, ions, and neutrals in the 20 to 400 keV energy range at 64 channels. It has a temporal resolution of 1 Hz and a spectral resolution of 6.25 keV for the linear mode and 2 to 24.32 keV for the pseudo-log mode. In addition, the MEPD has MEPD A and MEPD B telescopes with a field of view of 15° × 70°, which observe particles parallel and perpendicular to the local geomagnetic field, respectively. The HEPD measures electrons in the energy range of 0.35 to 2 MeV and protons in the energy range of 3 to 20 MeV. Its temporal resolution is 32 Hz, and its spectral resolution is approximately 100 keV at 1 MeV. The HEPD consists of three telescopes, each of which has a field of view of 33.4°.

Telescopes T0, T1, and T2 mounted on the HEPD observe particles with pitch angles of 0°, 45°, and 90°, respectively. The SRD data are provided in a hierarchical data format (HDF), which also includes information on the attitude and position of NEXTSat-1 and the local magnetic field. The files can be downloaded through the NEXTSat-1 homepage (http://n1isss.kaist.ac.kr/).

In this paper, we investigate the observations of a specific enhancement event of energetic particles in association with a substorm event and the radiation belt structure as seen by the SRDs. The paper is organized as follows. In section 2, we describe the particle injection seen in the MEPD observations. Then, in section 3, we present the electron distributions of the radiation belts obtained in the HEPD observations and analyze the spatial and temporal variations in the electron fluxes. We summarize our results in section 4.

2. OBSERVATIONS OF SUBSTORM INJECTION

The MEPD often observes substorm injections. Here, we introduce one example of these events that occurred on August 2, 2020. Fig. 1 shows the solar wind parameters from OMNIWeb (http://omniweb.gsfc.nasa.gov) data
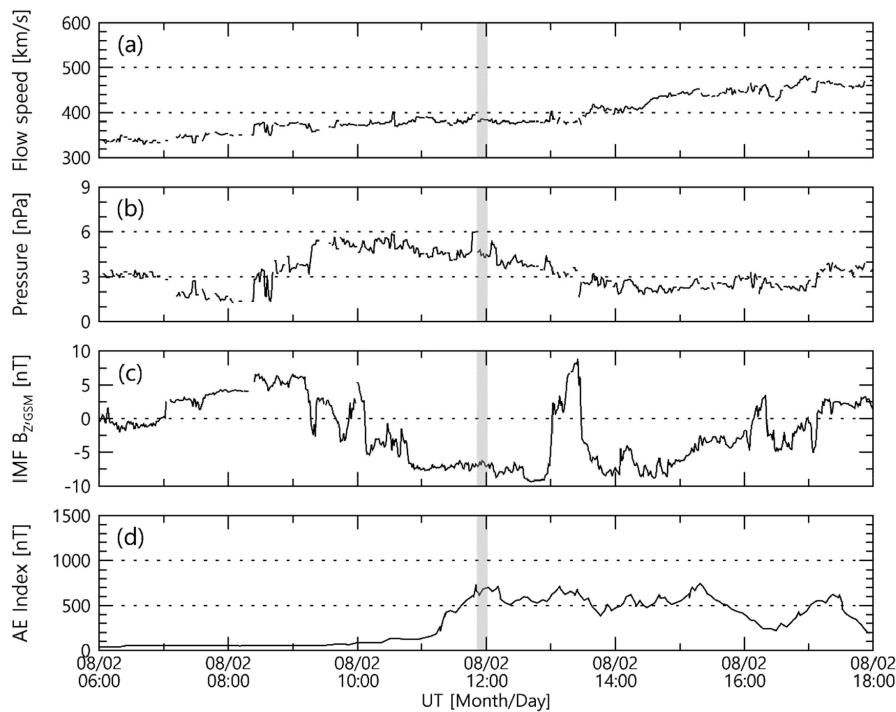
Fig. 1. Solar wind parameters and AE index on August 2, 2020. (a) Solar wind speed. (b) Solar wind dynamic pressure. (c) IMF B_z in geocentric solar magnetospheric (GSM) coordinates. (d) AE index. The shaded boxes correspond to the observation interval of the MEPD shown in Fig. 2. IMF, interplanetary magnetic field; MEPD, Medium-Energy Particle Detector.

with a 1 min resolution and the AE index from the World Data Center for Geomagnetism, Kyoto (http://wdc.kugi. kyoto-u.ac.jp/) around the observation time of the MEPD (the shaded interval in Fig. 1 corresponds to the interval in Fig. 2). Immediately before the MEPD observation, the solar wind speed is below 400 km/s, and the solar wind dynamic pressure is between 5 and 6 nPa. Additionally, the interplanetary magnetic field (IMF) B_z is rather strongly southward (~–7 nT for > 1 hr), which is a favorable condition for substorm occurrence. Indeed, the AE index rises well up to ~700 nT by the time of the MEPD event observation, indicating the occurrence of a strong substorm.

Fig. 2 exhibits the MEPD observations from 11:51 to 12:01 UT on August 2, 2020. During this period, NEXTSat-1 is located in the auroral region corresponding to L > 6 and near the midnight sector. The L values in SRDs data were derived from the International Geomagnetic Reference Field model, which therefore may not well represent disturbed times. Each of the MEPD A and B telescopes carries four detectors, Detector 0, 1, 2, and 3. Since Detector 1 and 2 measure ions, electrons, and neutrals without distinction among species, we do not use them for this paper. We use the data from Detector 0 and 3 only, which measure the precipitating and trapped charged particles with distinction between species (electrons

by Detector 0 and protons by Detector 3, respectively). The MEPD A measurements clearly indicate enhancements of the precipitating fluxes of both species (though larger for electrons) at energies of tens of keV. The trapped particles are also observed through the MEPD B telescope, but the flux enhancements are seen primarily in a narrower energy band of electrons. We attribute these enhancements in particle fluxes measured by this LEO satellite to substorm injection that occurred in the magnetospheric equatorial region. The injected particles are considered a seed population that is accelerated to relativistic energies by wave-particle interactions (Jaynes et al. 2015).

In relation to the MEPD observations, we confirmed substorm signatures through Geostationary Operational Environmental Satellite system (GOES) 17 observations at geosynchronous orbit, as shown in Fig. 3. The spacecraft is located near postmidnight during the MEPD observation interval, as indicated by the gray shaded box in Fig. 3. We used 1 min resolution particle data from the Magnetospheric Particle Sensor – High energy range (MPS-HI) and the Magnetometer (MAG) of the Space Environment *In-Situ* Suite (SEISS) onboard GOES 17 (https://www.ngdc.noaa. gov/). The MPS-HI detects protons with energies of 80 keV to 12 MeV and electrons with energies of 50 keV to 4 MeV
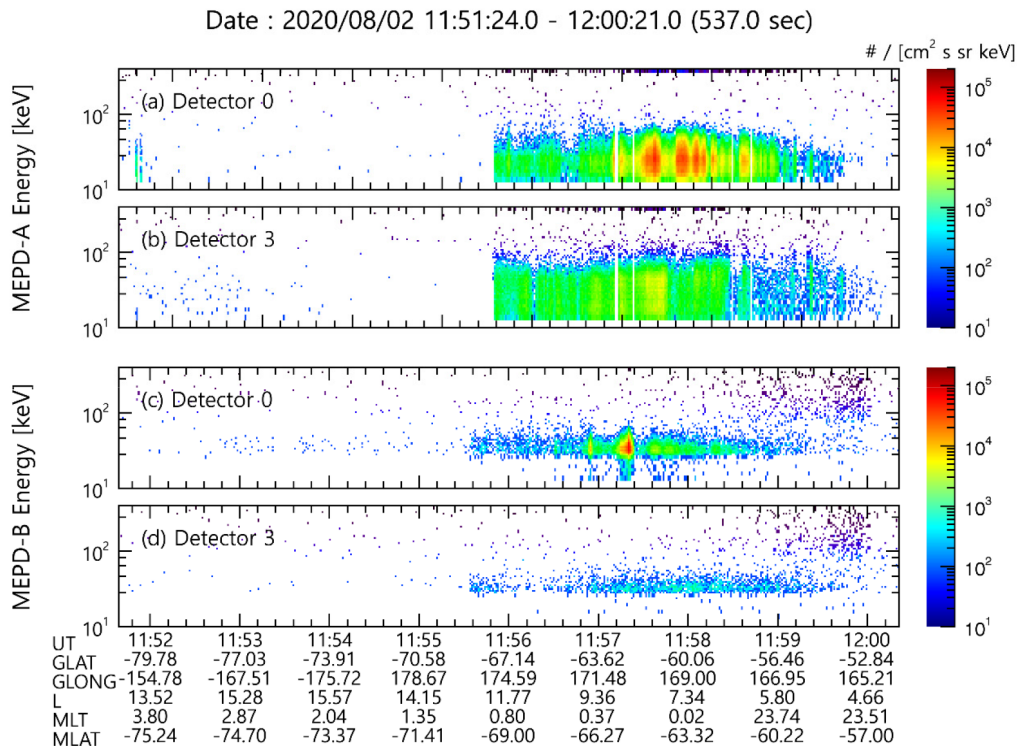
Fig. 2. MEPD observations from 11:51 to 12:01 on August 2, 2020. (a) Precipitating electron and (b) proton fluxes from the MEPD A telescope. (c) Trapped electron and (d) proton fluxes from the MEPD B telescope. MEPD, Medium-Energy Particle Detector.

GOES 17

2020-08-02
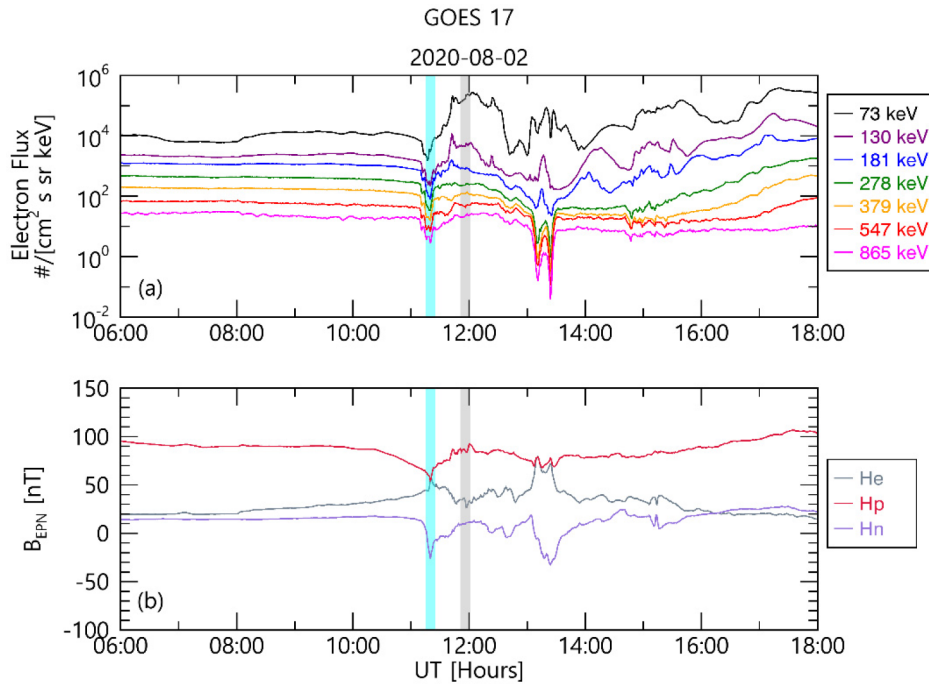
Fig. 3. Observations measured by GOES 17 on August 2, 2020. The upper panel shows the electron flux at selected energies from 73 keV to 865 keV. The lower panel shows the magnetic field in EPN coordinates. The shaded boxes (gray) correspond to the observation interval of the MEPD shown in Fig. 2. The shaded boxes (cyan) highlight flux dropouts caused by magnetic field stretching. GOES, Geostationary Operational Environmental Satellite system; EPN, Earth Polar Normal; MEPD, Medium-Energy Particle Detector.

and > 2 MeV via five telescopes. The MAG data are provided in Earth Polar (Parallel) Normal (EPN) coordinates, where the P-axis is normal to the orbit plane pointing northward, the E-axis points earthward, and the N-axis is in the eastward direction, completing the right-handed system (Kress et al. 2020; Loto'aniu et al. 2020).

In Fig. 3(a), flux dropouts are identified, as marked by the cyan box at ~11:10–11:20 UT, and they are then followed by electron flux increases immediately after substorm onset. The flux enhancements appear strongest at 73 keV and 130 keV, weak at 181 keV, and insignificant at the other higher energies. Fig. 3(b) shows the typical magnetic signatures of the substorm phenomena, that is, magnetic field stretching followed by dipolarization. The former is characterized primarily by an increase in the He component and a decrease in the Hp component, and the latter is characterized by an increase in the Hp component and a decrease in the He component. Note that the flux dropouts in panel (a) are caused by the magnetic field stretching and the dipolarization is responsible for the flux increases, part of which is what was observed by the MEPD in Fig. 2. Incidentally, there is another subsequent event of flux and magnetic field changes after 13 UT. This should be regarded as a separate event independent of the particle observations

by the MEPD in Fig. 2. We remark that a quantitatively precise comparison between the particle measurements by GOES 17 and NEXTSat-1 is nontrivial. Nevertheless, the MEPD observations can be used in conjunction with observations by other satellites, such as GOES spacecraft, which enables us to perform more specific studies.

3. OBSERVATIONS OF THE RADIATION BELT ELECTRON DISTRIBUTION

We present the radiation belt electrons over a wide energy range for a short interval (one full coverage of the L range of ~2 to 6) and a far longer-term period (~1.5 yr). Fig. 4 shows the observations of electrons with a 90° pitch angle for the short period during which the satellite passed through the inner radiation belt, the slot region, and the outer radiation belt. Note that the color bar ranges of the two detectors are different. In the region of L ~2.5 to 3.5, electrons with energy > ~500 keV are practically absent, confirming the well-known slot region. In L > ~3.5, the HEPD confirms the existence of the outer radiation belt with two distinguished populations: one centered at ~1 MeV and L ~3.9 and another at ~0.5 MeV and L ~5.3. The HEPD observations cover the

Date : 2020/10/24 11:29:55.0 - 11:38:53.0 (538.0 sec)
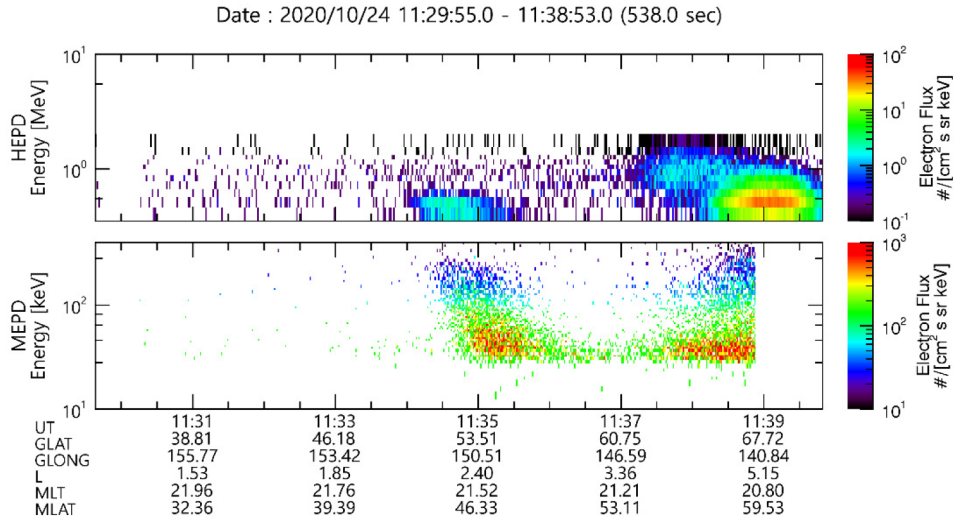
Fig. 4. Energy spectrum of electrons with a 90° pitch angle on October 24, 2020. The upper panel is the HEPD observation, and the lower panel is the MEPD observation. Note that the different energy units are used for HEPD and MEPD plots. HEPD, High-Energy Particle Detector; MEPD, Medium-Energy Particle Detector.

energy range of electrons in the outer radiation belt up to < 2 MeV, whereas the MEPD observations show the existence of energetic electrons from ~30 keV to 400 keV in the same region (but in this specific example, the MEPD observations are not available for L > ~5).

Next, Fig. 5 shows the Dst index, integrated electron flux with energy > 2 MeV observed by GOES 17, and the electron fluxes measured at 1,420 keV, 820 keV, and 505 keV by the HEPD 90° telescope for a long-term period of ~1.5 yr from July 2019. Overall, the HEPD observations reveal the outer radiation belt centered at L ~4–6 depending on the energy and geomagnetic activity level (Although not shown here, we confirmed that the overall structure of the outer radiation belt observed by HEPD is consistent with that seen by the Radiation Belt Storm Probes (RBSP) until the middle of October in 2019 (after which the RBSP observations are not available)). We recognize that the radiation belt electron fluxes at all energy channels are strongly enhanced occasionally in 2019 and the second half of 2020 when weak to moderate storms occur. In contrast, the level of electron flux is weaker than normal during the other times of weaker Dst conditions, most prominently from May to July 2020. In particular, the electron flux at 1,420 keV is reduced to the background level around this time, implying a near loss of the outer radiation belt. This trend is also observed for the > 2 MeV electron flux from GOES 17, as shown in Fig. 5(b). A similar loss that occurred in 2009 has been reported during unusually weak solar wind conditions (Lee et al. 2013). This should be due to loss mechanisms such as wave-particle interactions that occurred more dominantly than source

mechanisms. Furthermore, a comparison of Fig. 5(c)–(e) indicates that the inner edge of the outer radiation belt tends to lie at lower L values for lower energies, which is consistent with the previous study of Reeves et al. (2015).

Finally, we compare the inner edge of the outer radiation belt with the plasmapause location. For this, we superposed the Kp index and the plasmapause location in L (L_{pp}) on the electron flux data for two energies, as shown in Fig. 6. The L_{pp} model presented here was developed by Cho et al. (2015), which is determined by the solar wind speed and IMF B_z (see equation (1) of Cho et al. 2015). As seen in Fig. 6, when geomagnetic disturbances indicated by the Dst and Kp indices are large, the plasmapause is located at lower L values than in the quiet times. Overall, the inner edge of the outer radiation belt is consistent with L_{pp} at both energies. However, our visual inspection indicates that this coincidence is somewhat better for 505 keV than for 1,420 keV (Li et al. 2006). The reason for this energy dependence is likely because electron losses caused by plasmaspheric hiss and EMIC waves inside the plasmasphere are energy-dependent (e.g., Lee 2019; Kim et al. 2020). Although there have been a few studies that suggest sub-MeV electron losses by EMIC wave scattering, precipitation loss due to EMIC waves is more significant for higher energy electrons, primarily > 2 MeV (Summers & Thorne 2003; Shprits et al. 2016). On the other hand, plasmaspheric hiss can interact with sub-MeV electrons efficiently. Thus, we suggest that the inner edge of the outer radiation belt at sub-MeV energies is predominantly determined due to scattering by hiss waves and the effect of EMIC waves may be relatively weaker.
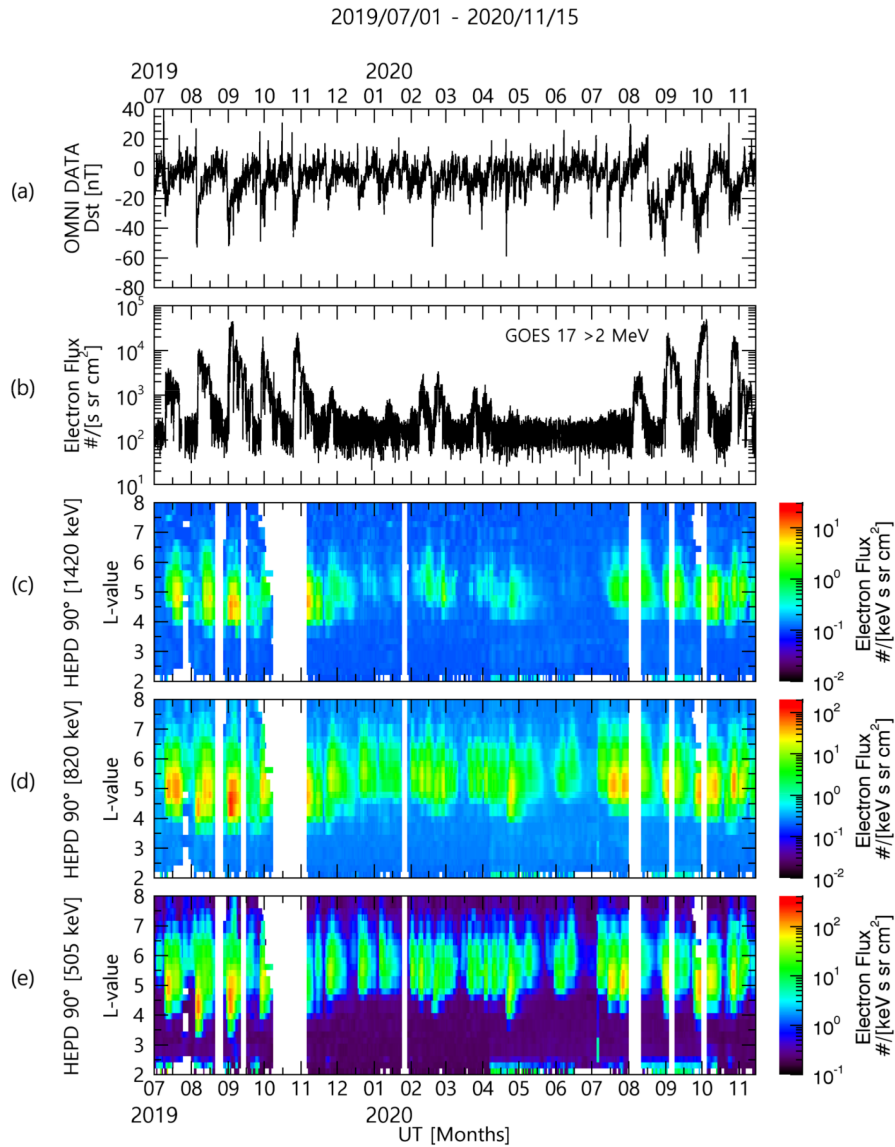
Fig. 5. Observations from July 2019 to November 2020. (a) Dst index. (b) > 2 MeV electron flux from GOES 17. (c)–(e) Electron fluxes at 1,420 keV, 820 keV, and 505 keV from the HEPD. GOES, Geostationary Operational Environmental Satellite system; HEPD, High-Energy Particle Detector.

Additionally, we identify a few times (middle of July, early September 2019 and middle of October 2020) when the 1,420 keV electrons penetrate into the plasmasphere. This is possibly because, according to Lee et al. (2013), the loss time scale for the relativistic electrons is longer than the outward expansion time scale of the plasmasphere.

4. CONCLUSIONS

In this work, we have analyzed some specific examples of energetic particle observations by the SRDs onboard NEXTSat-1. First, we investigated a substorm injection event based on the MEPD data and GOES 17 data. Both the parallel and perpendicular telescopes of the MEPD observed particle flux enhancements, which we attributed to substorm injection at energies of tens of keV, as observed by GOES 17. In particular, the fluxes at the MEPD are more strongly enhanced at the pitch angle of 0° than 90°, implying enhanced precipitation after the substorm onset. The occurrence of the substorm was confirmed by the typical signatures of magnetic field stretching and subsequent dipolarization and of particle flux dropout followed by enhancement at GOES 17.
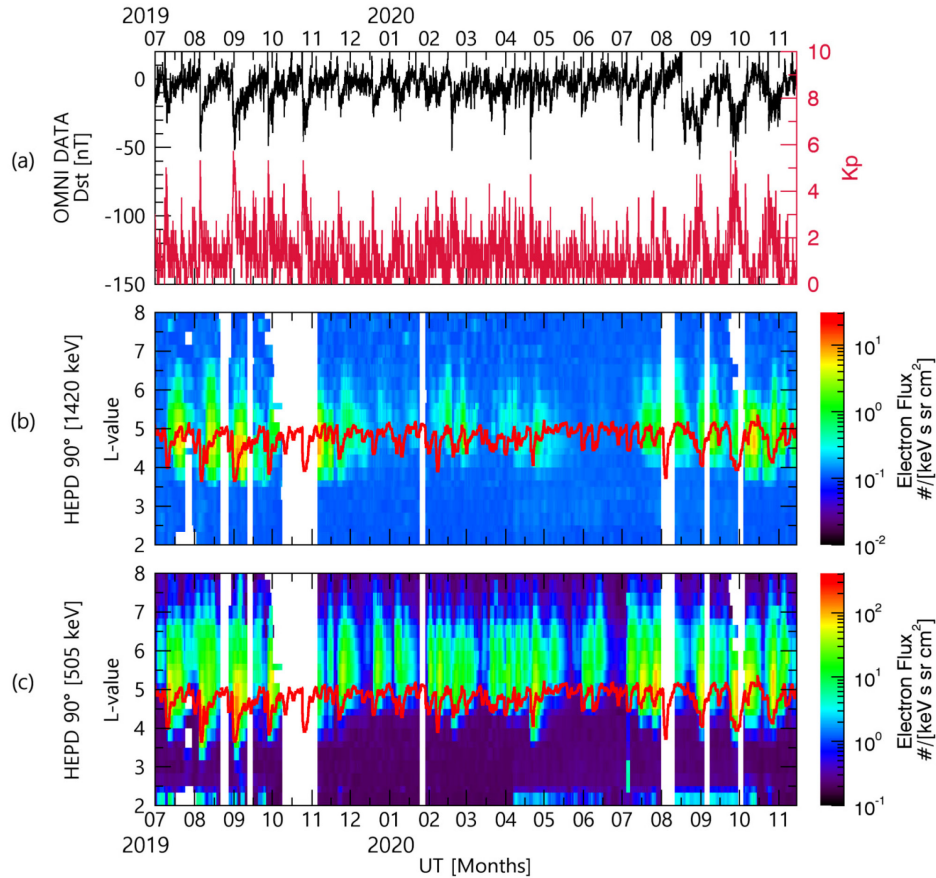
Fig. 6. Observations from July 2019 to November 2020. (a) Dst (black) and Kp (red) indices. (b)–(c) Electron fluxes at 1,420 keV and 505 keV from the HEPD. The red lines in (b) and (c) indicate the plasmapause L values, L_{pp}, determined by the model of Cho et al. (2015).

Additionally, we have presented the electron distributions in the radiation belts observed by both the MEPD and HEPD. As shown in Fig. 4, we could identify the energy-dependent slot region structure where electrons with > 500 keV energy were practically absent but lower energy electrons existed and the energy-dependent outer radiation belts for electron energies from hundreds of keV to a few MeV. Moreover, based on the electron fluxes as a function of time and L value at several energy channels, we have confirmed the typical structure and temporal and spatial variations of the outer radiation belt electron fluxes as measured by the HEPD, which is overall consistent with geomagnetic disturbance conditions. Additionally, the inner edge of the outer radiation belt is found to be overall consistent with the model plasmapause locations L_{pp}, but the agreement differs for different electron energies. When comparing the L_{pp} model developed by Cho et al. (2015) with the inner edge at each energy channel, somewhat better agreement is found at subrelativistic energy. A few instances are also identified where relativistic electron penetration

into the plasmasphere occurred. These results imply the significance of the role of wave-particle interactions inside the plasmasphere with an energy dependence. Based on the reported observations, we expect that the SRD data will be well utilized in many aspects to study the inner magnetosphere and near-tail dynamics in concert with other satellites.

ACKNOWLEDGMENTS

ORCIDS

Ji-Hyeon Yoo   https://orcid.org/0000-0002-2081-076X
Dae-Young Lee   https://orcid.org/0000-0001-9994-7277
Eojin Kim   https://orcid.org/0000-0003-4518-8468
Hoonkyu Seo   https://orcid.org/0000-0002-0683-7835
Kwangsun Ryu   https://orcid.org/0000-0001-8550-4213
Kyung-Chan Kim   https://orcid.org/0000-0002-1488-4375
Kyoungwook Min   https://orcid.org/0000-0002-1394-9341
Jongdae Sohn   https://orcid.org/0000-0002-6572-622X
Junchan Lee   https://orcid.org/0000-0003-1100-8852
Jongho Seon   https://orcid.org/0000-0001-6952-656X
Kyung-In Kang   https://orcid.org/0000-0002-8806-8098
Seunguk Lee   https://orcid.org/0000-0001-8045-6398
Jaeheung Park   https://orcid.org/0000-0002-1272-508X
Goo-Hwan Shin   https://orcid.org/0000-0002-7712-2511
SungOg Park   https://orcid.org/0000-0002-0363-6579

REFERENCES

Cho J, Lee DY, Kim JH, Shin DK, Kim KC, et al., New model fit functions of the plasmapause location determined using THEMIS observations during the ascending phase of solar cycle 24, J. Geophys. Res. Space Phys. 120, 2877-2889 (2015). http://doi.org/10.1002/2015JA021030

Choi CR, Sohn J, Lee JC, Seo YM, Kang SB, et al., Scientific missions and technologies of the ISSS on board the NEXTSat-1, J. Astron. Space Sci. 31, 73-81 (2014). http://doi.org/10.5140/JASS.2014.31.1.73

Jaynes AN, Baker DN, Singer HJ, Rodriguez JV, Loto'aniu TM, et al., Source and seed populations for relativistic electrons: their roles in radiation belt changes, J. Geophys. Res. Space Phys. 120, 7240-7254 (2015). https://doi.org/10.1002/2015JA021234

Kim E, Yoo JH, Kim HE, Seo H, Ryu K, et al., Initial operation and preliminary results of the instrument for the study of stable/storm-time space (ISSS) on board the next generation small satellite-1 (NEXTSat-1), J. Astron. Space Sci. 37, 209-218 (2020). https://doi.org/10.5140/JASS.2020.37.3.209

Kim KC, Shprits Y, Wang D, Quantifying the effect of plasmaspheric hiss on the electron loss from the slot region, J. Geophys. Res. Space Phys. 125 (2020). http://doi.org/10.1029/2019JA027555

Kress BT, Rodriguez JV, Onsager TG, The GOES-R space environment *in situ* suite (SEISS): measurement of energetic particles in geospace, in The GOES-R Series: a new generation of geostationary environmental satellites, eds. Goodman S, Schmit TJ, Daniels JM, Redmond RJ (Elsevier, Amsterdam, 2020), 243-250.

Lee DY, Recent progress in the theoretical understanding of relativistic electron scattering and precipitation by electromagnetic ion cyclotron waves in the Earth's inner magnetosphere, J. Astron. Space Sci. 36, 45-60 (2019). https://doi.org/10.5140/JASS.2019.36.2.45

Lee DY, Shin DK, Kim JH, Cho JH, Kim KC, et al., Long-term loss and re-formation of the outer radiation belt, J. Geophys. Res. Space Phys. 118, 3297-3313 (2013). http://doi.org/ 10.1002/jgra.50357

Lee J, Min K, Ryu K, Kang KI, Shin GH, et al., Space plasma detectors on NEXTSat-1 for ionospheric measurements, J. Korean Phys. Sci. 72, 1393-1401 (2018). https://doi.org/10.3938/jkps.72.1393

Li X, Baker DN, O'Brien TP, Xie L, Zong QG, Correlation between the inner edge of outer radiation belt electrons and the innermost plasmapause location, Geophys. Res. Lett. 33, L14107 (2006). http://doi.org/10.1029/2006GL026294

Loto'aniu PTM, Califf S, Redmon RJ, Singer HJ, Magnetic field observations from the GOES-R series, in The GOES-R Series: a new generation of geostationary environmental satellites, eds. Goodman S, Schmit TJ, Daniels JM, Redmond RJ (Elsevier, Amsterdam, 2020), 251-259.

Reeves GD, Friedel RHW, Larsen BA, Skoug RM, Funsten HO, et al., Energy-dependent dynamics of keV to MeV electrons in the inner zone, outer zone, and slot regions, J. Geophys. Res. Space Phys. 121, 397- 412 (2016). http://doi.org/10.1002/2015JA021569

Shin GH, Chae JS, Lee SH, Min KW, Sohn JD, et al., Operational concept of the NEXTSat-1 for science mission and space core technology verification, J. Astron. Space Sci. 31, 67-72 (2014). https://doi.org/10.5140/JASS.2014.31.1.67

Shprits YY, Drozdov AY, Spasojevic M, Kellerman AC, Usanova ME, et al., Wave-induced loss of ultra-relativistic electrons in the Van Allen radiation belts, Nat. Commun. 7, 12883 (2016). https://doi.org/10.1038/ncomms12883

Sohn J, Lee J, Min K, Lee J, Lee S, et al., HEPD on NEXTSat-1: a high energy particle detector for measurements of precipitating radiation belt electrons, J. Korean Phys. Soc. 72, 1086-1093 (2018). https://doi.org/10.3938/jkps.72.1086

Summers D, Thorne RM, Relativistic electron pitch-angle scattering by electromagnetic ion cyclotron waves during geomagnetic storms, J. Geophys. Res. 108, 1143 (2003). http://doi.org/10.1029/2002JA009489